



Coherent precipitation of cuboidal nanoparticles in $\text{Al}_1\text{Ti}_5\text{Zr}_4\text{Nb}_3\text{Ta}_3$ lightweight refractory high entropy alloy based on laser metal deposition

Xuanhong Cai^{a,b}, Qiuju Yang^b, Liufei Huang^{b,c}, Peilin Dong^{b,d}, Congcong Ren^b, Yuanfeng Zhou^b, Jinfeng Li^{b,*}, Qing Wang^a

^a School of Materials Science and Engineering, Dalian University of Technology, Dalian 116024, China

^b Institute of Materials, China Academy of Engineering Physics, Mianyang 621908, China

^c School of Mechanical Engineering, Xinjiang University, Urumqi 830017, China

^d School of Electronic Science and Engineering, University of Electronic Science and Technology of China, Chengdu 611731, China



ARTICLE INFO

Keywords:

Refractory high entropy alloy
Laser metal deposition
Coherent microstructure
Mechanical property

ABSTRACT

Usually, the Al-containing lightweight refractory high entropy alloys (RHEAs) prepared by casting require complex heat treatment to obtain BCC/B2 coherent microstructure, thereby achieving excellent room temperature (*RT*) and high temperature (*HT*) mechanical properties. In this work, we design a novel lightweight RHEA of $\text{Al}_1\text{Ti}_5\text{Zr}_4\text{Nb}_3\text{Ta}_3$ ($\rho = 7.46 \text{ g}\cdot\text{cm}^{-3}$) via the cluster formula approach and utilize high cooling rate and in-situ heat treatment effects of laser metal deposition (LMD) to directly obtain the BCC/B2 coherent microstructure with cuboidal BCC nanoparticles precipitated. The LMD-fabricated alloy exhibits good formability, with equiaxed grains ($\sim 38 \mu\text{m}$ in size) uniformly distributed along the deposition direction. Compared with the *RT* compressive yield strength of the as-cast alloy ($\sigma_{YS} = 1070 \text{ MPa}$), the LMD-fabricated alloy exhibits a notable enhancement by 50 % reached to 1600 MPa, which is attributed to the unique BCC/B2 coherent microstructure. Furthermore, this LMD-fabricated alloy possesses prominent elevated temperatures mechanical properties ($\sigma_{YS} = 1124 \text{ MPa}$ at 873 K and $\sigma_{YS} = 259 \text{ MPa}$ at 1273 K) due to the excellent thermal stability of the BCC/B2 coherent microstructure. The exceptional yield strength of the LMD-fabricated alloy is mainly ascribed to the grain boundary strengthening, dislocation strengthening, precipitation strengthening, and solid solution strengthening. The present work provides a new strategy for the design and fabrication of high-strength and high-plasticity RHEAs.

1. Introduction

High-entropy alloys (HEAs), or multi-principal element alloys (MPEAs) emerging as a novel frontier in the metal materials community that have garnered considerable interest because of their exceptional mechanical and functional properties [1–7]. The refractory high-entropy alloys (RHEAs) are a sub-class of HEAs holding high temperature (*HT*) softening resistance strength outperforms most superalloys, such as Haynes 230 and Inconel 718 [2,8,9]. For instance, the reported WMoNbTa and WMoNbTaV RHEAs exhibit the yield strength of $\sigma_{YS} = 405 \text{ MPa}$ and $\sigma_{YS} = 477 \text{ MPa}$ at 1600 °C, respectively [10,11]. However, these RHEAs composed of heavy elements (W, Nb, Ta, etc.) often exhibit a relatively higher density ($\rho > 10 \text{ g}\cdot\text{cm}^{-3}$), which significantly restricts their engineering applications [12]. Subsequently, the development of RHEAs is focused on reducing alloy density to meet the demanding service requirements of high specific strength in potential

aerospace applications. Consequently, the low-density Al, Cr, Ti, and Si are usually substituted for heavy elements (W, Nb, Ta, etc.) to form lightweight RHEAs with a density of less than $8 \text{ g}\cdot\text{cm}^{-3}$, in which the second phases including the ordered B2 phase, hexagonal Laves phase and Al_3Zr_5 phase could be precipitated into the BCC matrix as the secondary strengthening phases [5,13]. Despite the considerable enhancement in the strength of the lightweight RHEAs, a notable degradation in plasticity occurs due to the precipitation of coarse particles, which is attributed to the semi-coherent or non-coherent relationship between the second phases and the BCC matrix [12,13]. Interestingly, in Al-containing lightweight RHEAs, the ordered B2 phase tends to coexist with the disordered BCC phase to form the BCC/B2 coherent microstructure comparable to that (FCC- γ/γ') of Ni-based superalloys, which renders alloys with ultrahigh strength at both *RT* and *HT* [8,9,14–19]. For instance, the $\text{AlMo}_{0.5}\text{NbTa}_{0.5}\text{TiZr}$ RHEA has significantly improved mechanical properties, with a compressive yield

* Corresponding authors.

E-mail addresses: lijinfeng305@126.com (J. Li), wangq@dlut.edu.cn (Q. Wang).

strength of $\sigma_{YS} = 2193$ MPa at 298 K, and $\sigma_{YS} = 745$ MPa at 1273 K, respectively, which is ascribed to its coherent microstructure of cuboidal BCC nanoparticles in the B2 matrix [14]. However, the formation of a uniform BCC/B2 coherent microstructure typically requires complex heat treatment processes [14–19], which often result in the precipitation of brittle phases (Al_xZr_y , Laves, etc.), thereby deteriorating the mechanical properties of the alloys [20–24]. Moreover, the inherently slow cooling rate associated with conventional arc-melting process often results in the formation of coarse grain structures and severe elemental segregation within the alloys [4,25,26], posing significant challenges for the fabrication of RHEAs through traditional methods.

Laser metal deposition (LMD), as a typical metal additive manufacturing (AM) technique, is a more desirable methods to process RHEAs given the ultrafast heating rates and cooling rates, with the latter reaching $10^3 - 10^8$ K·s $^{-1}$ at the solid/liquid interface within a small-size melt pool [27]. The rapid melting and solidification are derived from the short interaction time between the concentrated energy and metal powders, resulting in refined microstructures and inhibiting the precipitation of the harmful brittle precipitates that are contributed to enhance the mechanical properties in the fabricated alloys [27]. For instance, the LMD-fabricated $Hf_{10}Nb_{12}Ti_{40}V_{38}$ RHEAs exhibits the elements of Hf, Nb, Ti, and V uniformly-distributed at both grain boundaries and grain interiors, which is ascribed to the rapid solidification effectively reduce the segregation [28]. Also, the LMD-fabricated $Ti_{41}V_{27}Hf_{13}Nb_{13}Mo_6$ alloy shows suppressed the precipitation of needle-like Hf-rich HCP phases at grain boundaries, leading to an enhancement in room temperature (RT) elongation to fracture to $\delta \sim 11\%$ while retaining a high tensile yield strength of $\sigma_{YS} = 1195$ MPa [29]. However, laser additive manufactured lightweight RHEAs alloys with the BCC/B2 coherent microstructure have rarely been reported [30–32]. Especially, the LMD-fabricated $Al_{10}Ti_{31.5}Zr_{45}Nb_{13.5}$ lightweight RHEAs exhibits excellent properties with a compressive yield strength of $\sigma_{YS} = 1456$ MPa and a compression strain to fracture of $\delta \sim 56\%$, as compared with $\sigma_{YS} = 1066$ MPa and $\delta \sim 45\%$ for the as-cast alloy, due to B2 nanoparticles are coherently precipitated into BCC matrix [31]. Nevertheless, the BCC/B2 coherent microstructure in the LMD-fabricated lightweight RHEAs exhibits a non-uniform distribution [31,32]. For instance, the LMD-fabricated $AlMo_{0.5}NbTa_{0.5}TiZr$ alloy consists of the BCC/B2 coherent microstructure and a higher content of indendritic HCP phases compared to the as-cast alloy, resulting in a compressive yield strength of $\sigma_{YS} = 1887$ MPa at RT is not superior to that ($\sigma_{YS} = 2000$ MPa) of the as-cast alloy [32]. Therefore, achieving the BCC/B2 coherent microstructure in LMD-fabricated RHEAs requires not only optimization of the laser additive manufacture process but also a rational compositional design.

In previous studies, we employed the cluster formula of Al_2M_{14} to design a novel series of RHEAs in the Al - Ti - Zr - Nb - Ta system, where M represents adjustable combinations of Ti, Zr, Nb, and Ta, realizing the regulation of the BCC/B2 coherent microstructure [33,34]. Especially, the $Al_2Ti_6Zr_2Nb_3Ta_3$ ($M_{14} = Ti_6Zr_2Nb_3Ta_3$) alloy has both a high compressive yield strength of $\sigma_{YS} = 1193$ MPa and an extremely high combustion calorific of $Q = 10240$ J·g $^{-1}$, showing its promising application as novel energetic structural materials [33]. Here, Al is reduced in order to avoid the precipitation of brittle Al_xZr_y phases [35]. Meanwhile, a proper regulation of Ti and Zr can tailor the lattice misfit between the BCC and B2 phases for the formation of cuboidal nanoparticles [33,34,36]. Therefore, a novel $Al_1Ti_5Zr_4Nb_3Ta_3$ RHEA with a low density of $\rho = 7.46$ g·cm $^{-3}$ was designed. Firstly, the single-track experiments via LMD were carried out to determine the optimum process window. And the single-wall alloy with uniform distributed equiaxed grains along the deposition direction was fabricated successfully under the optimized process parameters. Then, the microstructures and mechanical properties of the LMD-fabricated alloy are characterized and tested, respectively. In comparison, a detailed analysis of the microstructures and mechanical properties of the as-cast alloy was also provided. Subsequently, the formation of microstructures mechanism and the

strengthening mechanism of the LMD-fabricated alloy was discussed.

2. Materials and experimental procedures

2.1. Preparation of the as-cast alloy and pre-alloyed powders

Ingots weighing 100 g of $Al_1Ti_5Zr_4Nb_3Ta_3$ were fabricated in the vacuum arc-melting furnace under an argon atmosphere. Commercially pure metallic ingredients (the purity of metal elements: 99.99 wt%) were used as raw materials. Moreover, an ingot weighing 2.5 kg were melted and subsequently cast into an electrode bar with a length of 180 mm, upper inner diameter of 60 mm, and bottom inner diameter of 50 mm. Powders with different sizes in a range of 53 – 120 μ m was prepared using the plasma rotating electrode process (PREP) [37]. To ensure the fluidity of powder feeding during AM process, the powders with approximately 160 mesh were selected through sieving.

2.2. LMD fabrication

Pre-alloyed powders were heated up to 393 K for 2 h and cooled down to RT in a vacuum chamber to remove water vapor before use. The processing chamber was filled with high-purity argon and the oxygen content was maintained below 1000 ppm in the fabrication process, while the powder was delivered in to the laser molten on a Zr substrate through a coaxial powder delivery system. During the fabrication process, ytterbium-doped fiber laser unit with a wavelength of 1070 nm and a spot diameter of 1.8 mm was used as the power source. Before fabricating the single-wall samples, single-track experiments were carried out with a wide range of process parameters to determine the optimum process window, as shown in Fig. 1(a). Optical micrographs of the transverse section of single-tracks specimens fabricated according to the Table 1 orthogonal experiment parameters are shown in Fig. 1(b). In the AM process, the higher laser power and scanning speed would lead to a higher amount of spattering, which is harmful to obtaining the optimal alloy sample. As a result, the moderate laser power $P = 1400$ W and laser scanning rate $V = 500$ mm/s (No.5, indicated by green box) are sufficient to obtain perfect molten pool morphology with the track height (Δh) of 0.36 mm and the track width (Δx) of 5 mm, as presented in Fig. 1(b). After layer-by-layer deposition, a single-wall sample with the dimensions of 50 × 35 × 5 mm (length × height × width) was obtained, as shown in Fig. 1(c, d). The alloy was fabricated successfully under the optimized processing condition, showing excellent formability without any cracks or warps, as shown in Fig. 1(d) and Supplementary Fig. S1. Moreover, Fig. 1(e) shows the different parts of the LMD-fabricated alloy and then they will be characterized.

2.3. Material characterizations

The pre-alloyed powders were fabricated by SLPA-N50 PREP equipment. The chemical compositions of the powder were determined by Agilent 7700 inductively coupled plasma optical emission spectrometer (ICP-OES). The particle size of the powder was measured by Microtrac S3500 laser particle size analyzer. The macroscopic morphology of the single-tracks and single-walls were examined by Nikon ECLIPSE LV 150 N optical microscope (OM). Microhardness of LMD-fabricated alloy was measured using the HVS-1000 Vickers hardness tester under a load of 500 g and a holding time of 15 s. The crystalline structures of powders and alloys were identified using a Bruker D8 X-ray diffractometer (XRD) with the $Cu K\alpha$ radiation ($\lambda = 0.15406$ nm). The microstructures of the powders and alloys were examined by Thermo Scientific Helios 5 CX scanning electron microscopy (SEM) and JXA-8530F PLUS electronic probe micro-analyzer (EPMA). Electron backscatter diffraction (EBSD) measurements were performed using Thermo Scientific Helios 5 CX SEM equipped with an Oxford Symmetry detector, where the samples were prepared by argon ion beam polishing. The nanoparticles were further examined using FEI

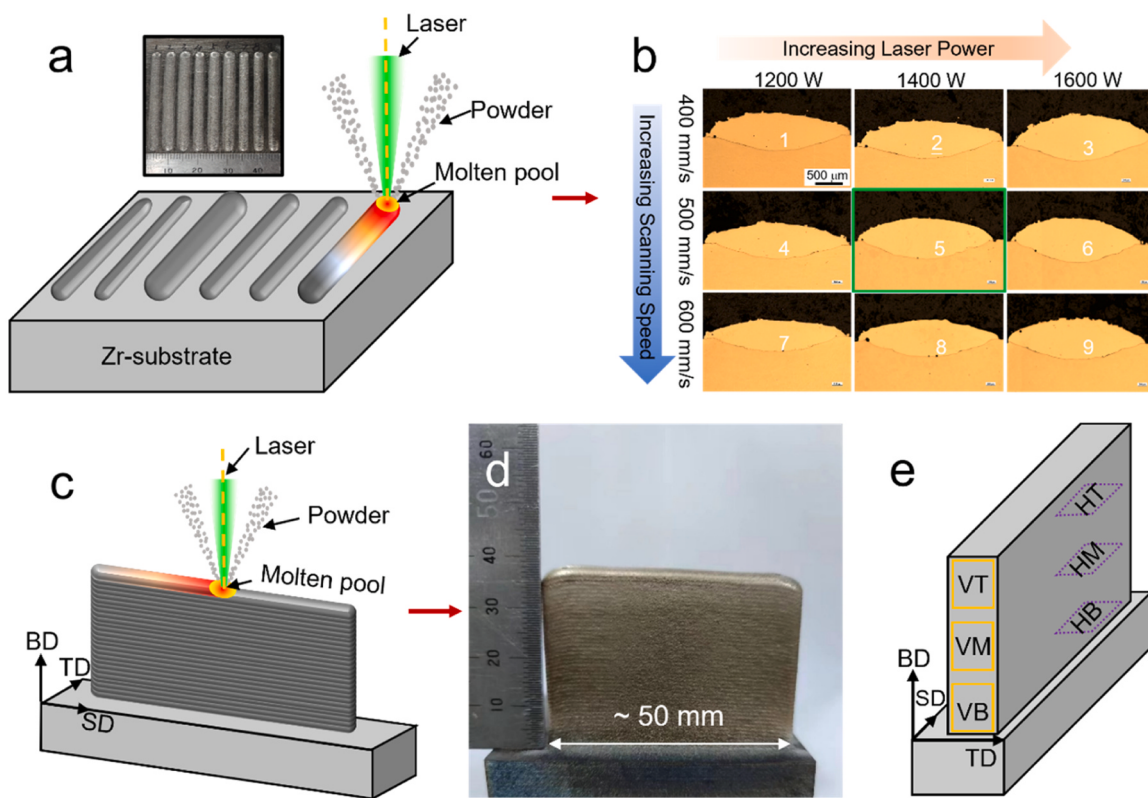


Fig. 1. (a) The schematic illustration of single-track experiments to determine the optimum process, (b) the optical micrographs of the single-tracks with different P (1200 – 1600 W) and V (400 – 600 mm/s), (c) the schematic illustration of LMD process, where SD, BD, and TD indicating laser scanning direction, building direction, and transverse direction, respectively, (d) the single-wall specimen, (e) the schematic illustration of different parts in the single-wall, where the horizontal cross-sections of bottom, middle, and top layers parallel to SD-TD plane, referred as to HB, HM, and HT, and the vertical cross-sections of bottom, middle, and top layers parallel to BD-TD plane, referred as to VB, VM, and VT, respectively.

Table 1
Orthogonal experimental parameters of fabricated single-tracks.

P/V	1200 W	1400 W	1600 W
400 mm/s	1	2	3
500 mm/s	4	5	6
600 mm/s	7	8	9

Talos F200X scanning transmission electron microscopy (STEM) equipped with a high-angle annular dark field detector (HAADF) and Super-X energy dispersive X-ray spectroscopy (EDS) detector at an operating voltage of 200 kV. TEM specimens were prepared using RL-2 type electrolytic double-spray, where the etching solution for double-spray was composed of 6 % HClO_4 + 35 % $\text{CH}_3(\text{CH}_2)_3\text{OH}$ + 59 % CH_3OH . Moreover, equilibrium phase diagrams were calculated by Pandat software with the latest PanRHEA2024_TH+MB thermodynamics database.

2.4. Mechanical property testing

Uniaxial compression tests were conducted on a UTM5504 Material Test System (MTS) with a strain rate of $1 \times 10^{-3} \text{ s}^{-1}$ at both RT and HT. The compressive specimens were machined from the as-cast and LMD-fabricated alloys bulk with the dimensions of $3 \times 4.8 \text{ mm}$ (diameter \times height). Three samples for each state were tested to ensure reliability.

3. Results

3.1. Powder characteristics

The compositions of the pre-alloyed powder are $\text{Al}_{6.50}\text{Ti}_{32.50}\text{Zr}_{25.70}\text{Nb}_{17.30}\text{Ta}_{18.00}$ (at%) determined by ICP-OES, which is almost consistent with the nominal design composition of $\text{Al}_{6.25}\text{Ti}_{31.25}\text{Zr}_{25.00}\text{Nb}_{18.75}\text{Ta}_{18.75}$ (at%) and it is listed in Table 2. Subsequently, the morphology of the representative pre-alloyed $\text{Al}_1\text{Ti}_5\text{Zr}_4\text{Nb}_3\text{Ta}_3$ powders is in a spherical shape with desired flowability, which is beneficial for the LMD process to fabricate alloys, as observed in Fig. 2(a). The corresponding EDS mapping show that the Al, Ti, Zr, Nb, and Ta elements are uniformly distributed in the surface of the powder, as shown in Fig. 2(b). And the median grain size (D_{50}) of the pre-alloyed powder is approximately of $36 \mu\text{m}$, as displayed in Fig. 2(c). However, the analyses of the XRD indicate that the powder is constituted of two BCC structure phases, namely BCC1 and BCC2, as evidenced by the splitting in diffraction peaks of the BCC phase (Fig. S2(a)), which is primarily attributed to the formation of dendrite microstructure within the powder (Fig. S2(b, c)). The EDS mapping exhibits that the bright dendritic BCC1 phases are enriched by Nb and Ta, while the dark interdendritic BCC2 are segregated by Al, Ti, and Nb, and the specific compositions are listed in Table 3.

Table 2
The nominal design and actual compositions of the pre-alloyed powder.

Composition (at%)	Al	Ti	Zr	Nb	Ta
Nominal	6.25	31.25	25.00	18.75	18.75
Actual	6.50	32.50	25.70	17.30	18.00

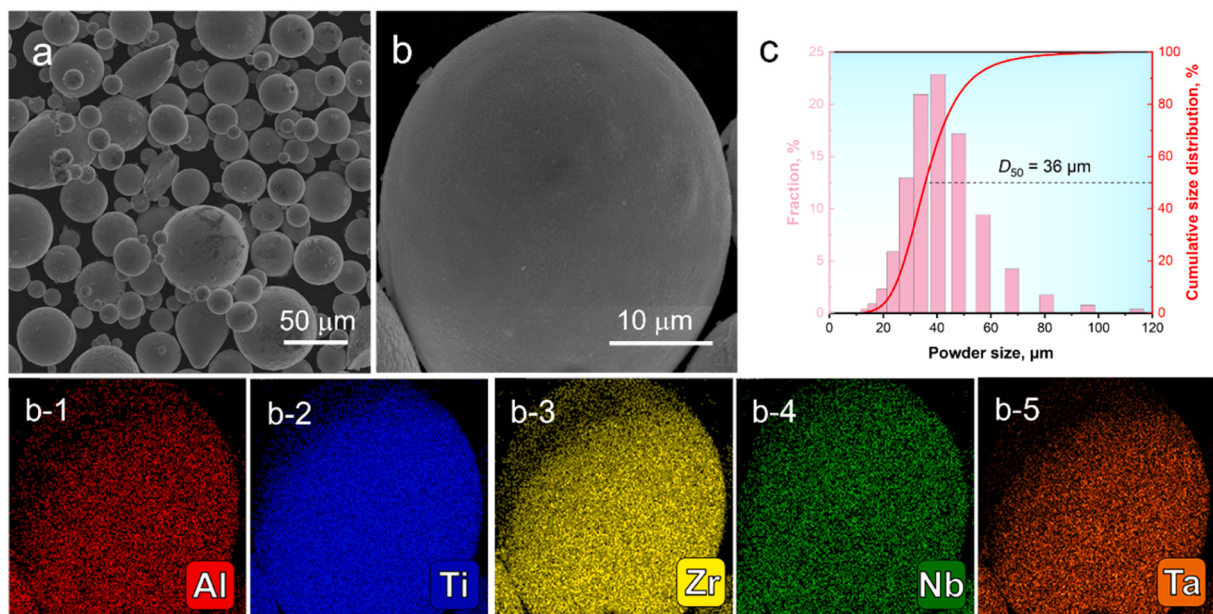


Fig. 2. (a) The pre-alloyed powder morphology, (b) the magnified image of the powder and the corresponding EDS mapping, (c) the cumulative particle size distribution of the powder.

Table 3

Related information of the phase constitution and elemental composition in the pre-alloyed powder, as-cast alloy, and LMD-fabricated alloy.

Alloy	Phase constitution	Elemental composition (at%)				
		Al	Ti	Zr	Nb	Ta
Powder	Dark phase	8.2	35.6	36.3	12.1	7.8
	Bright phase	4.2	31.4	19.6	22.5	22.3
As-cast	Dark phase	8.2	34.4	30.2	14.7	12.5
	Bright phase	5.7	33.2	21.6	18.9	20.7
LMD	Dark phase	8.2	35.5	29.1	14.3	12.9
	Bright phase	4.2	32.2	16.8	19.6	27.2
	Island-like BCC	3.8	35.5	12.9	21.6	26.2
	Cuboidal BCC	9.0	35.4	26.0	13.3	17.5
	B2 matrix	25.8	37.3	21.7	9.1	6.1

3.2. The microstructures of the LMD-fabricated and as-cast alloys

To understand the influence of LMD on the microstructure of the $\text{Al}_1\text{Ti}_5\text{Zr}_4\text{Nb}_3\text{Ta}_3$ RHEAs, a detailed characterization on phase constitutions and microstructural morphologies of the LMD-fabricated and as-cast alloys was conducted. Fig. 3(a-c) illustrate the reconstructed EBSD inverse pole figures (IPF) of the vertical-section zone (VB, VM, and VT) parallel to the BD-TD plane. It is evident that the fine equiaxed grains were uniformly distributed from bottom layers to top layers along the deposition direction. The corresponding grain size (d) were measured to be $d_{\text{VB}} = 31 \pm 13 \mu\text{m}$, $d_{\text{VM}} = 39 \pm 15 \mu\text{m}$, and $d_{\text{VT}} = 45 \pm 17 \mu\text{m}$, respectively, and the average grain size of the LMD-fabricated alloy was measured to be $38 \mu\text{m}$. Besides, the LMD-fabricated alloys exhibit a relatively random distribution of crystallographic orientation (Fig. S3(a-c)), which is different from the columnar grains in most additively manufactured alloys [38,39]. By contrast, the as-cast alloy exhibits coarse equiaxed grains with the grain size of $206 \mu\text{m}$, as shown in Fig. 3(d). And the detailed statistical distribution of grain size is presented in Fig. 3(e). The above results indicate that the LMD process can avoid the formation of columnar grain and effectively refine the grain size of the $\text{Al}_1\text{Ti}_5\text{Zr}_4\text{Nb}_3\text{Ta}_3$ RHEAs.

The further microstructure characterization results of the molten pool in the LMD-fabricated alloy reveal that the epitaxially grown bright equiaxed dendrite phases are uniformly distributed into the dark

interdendrite phases, as shown in Fig. 4(a-c). It can be clearly seen that the bright equiaxed dendrite phases in VB region are finer than those in the VM and VT zones. Especially, the as-cast alloy exhibit similar but coarser dendritic microstructure, as shown in Fig. 4(d). The corresponding EDS elemental mapping (Fig. 4(a-1, d-1)) show that these bright equiaxed dendrite phases are enriched by Nb and Ta, while Al, Ti, and Zr are segregated in the dark interdendrite phases, and the specific compositions are listed in Table 3. This indicates that Nb and Ta with high-melting points solidify first, while Al, Ti, and Zr with low-melting points crystallize later during solidification. Moreover, the XRD patterns of the LMD-fabricated (VB, VM, and VT) and the as-cast alloys show single diffraction peaks of BCC structure, indicating both the bright equiaxed dendrite and dark interdendrite are BCC phases, as shown in Fig. 4(e). Also, the HT and HB samples of the LMD-fabricated alloy (Fig. 1(e)) exhibit the same microstructures as the VT and VB samples, as displayed in Fig. S4.

The layer-by-layer deposition for LMD process may result in the microstructural heterogeneity between the molten pool and remelting zones. To explore the microstructure of the remelting zones of the LMD-fabricated alloy, Fig. 5 displays typical morphology spanning multiple molten pools and corresponding EPMA elemental mapping of the representative VM sample. It is found that the molten pools (indicated by the yellow box) and remelting zones (indicated by the blue box) are alternately distributed, as shown in Fig. 5(a). The microstructures of remelting zones exhibit remarkable consistency with those of the molten pools consisted of dark interdendrites and bright equiaxed dendrites, as demonstrated in Fig. 5(b, c). EPMA elemental mapping (Fig. 5(c-1)) shows that the bright equiaxed dendrite phases of remelting zone are enriched in Ta and a small amount of Nb, whereas Al, Ti, and Zr partition mainly to the dark interdendrite phases, which is consistent with the results of EDS (Fig. 4(a-1)). The microstructural homogeneity throughout different regions strongly suggests the uniform nature of the LMD-fabricated $\text{Al}_1\text{Ti}_5\text{Zr}_4\text{Nb}_3\text{Ta}_3$ alloy. In addition, it is found that bright nanoparticles (indicated by the red arrows) are precipitated at both grain interiors and grain boundaries, as shown in the inset of Fig. 5(b), which will be further analyzed by TEM.

To further reveal the morphology and crystal structure of the nanoparticles, the representative TEM analyses of the middle part (VM) were performed. The high-angle annular dark field (HAADF) image reveals that the bright cuboidal nanoparticles are precipitated in the dark

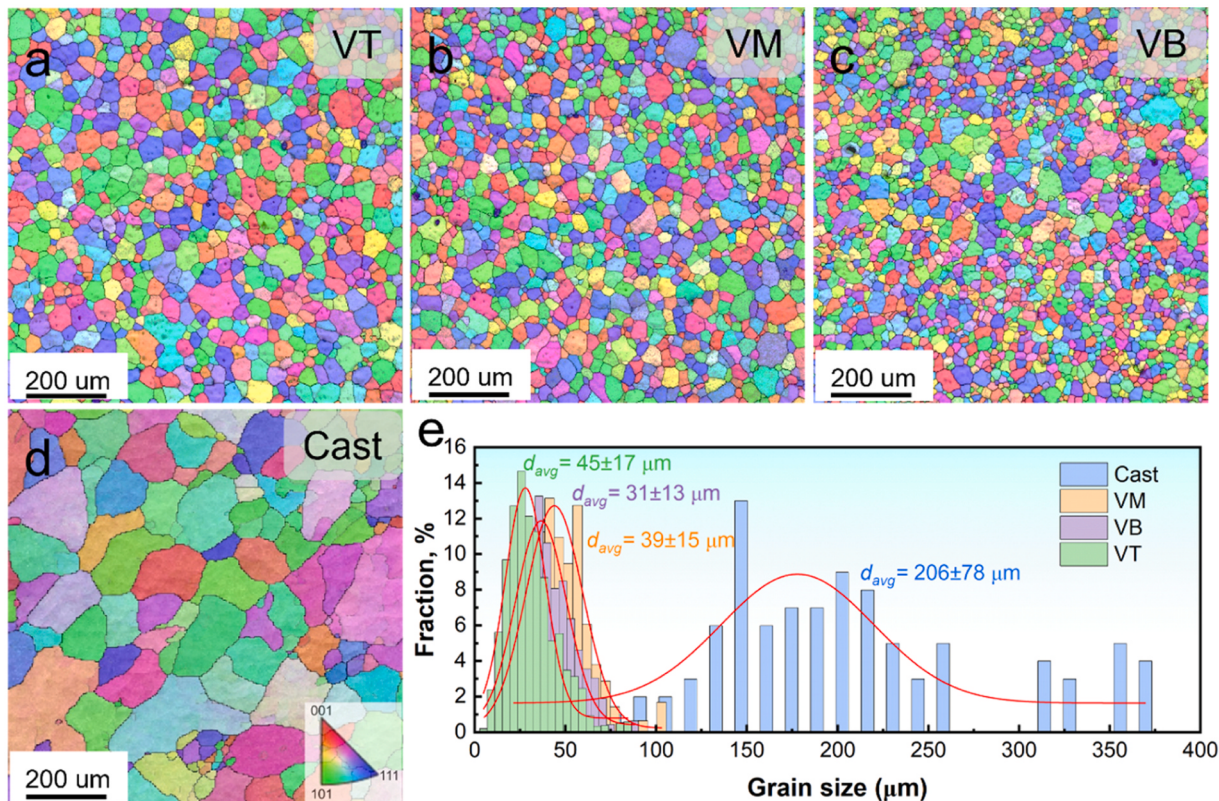


Fig. 3. The grain distribution of the LMD-fabricated and as-cast alloys. (a-d) EBSD IPF maps of the LMD-fabricated alloy (VT, VM, and VB) and the as-cast alloy, (e) the distribution of grain size.

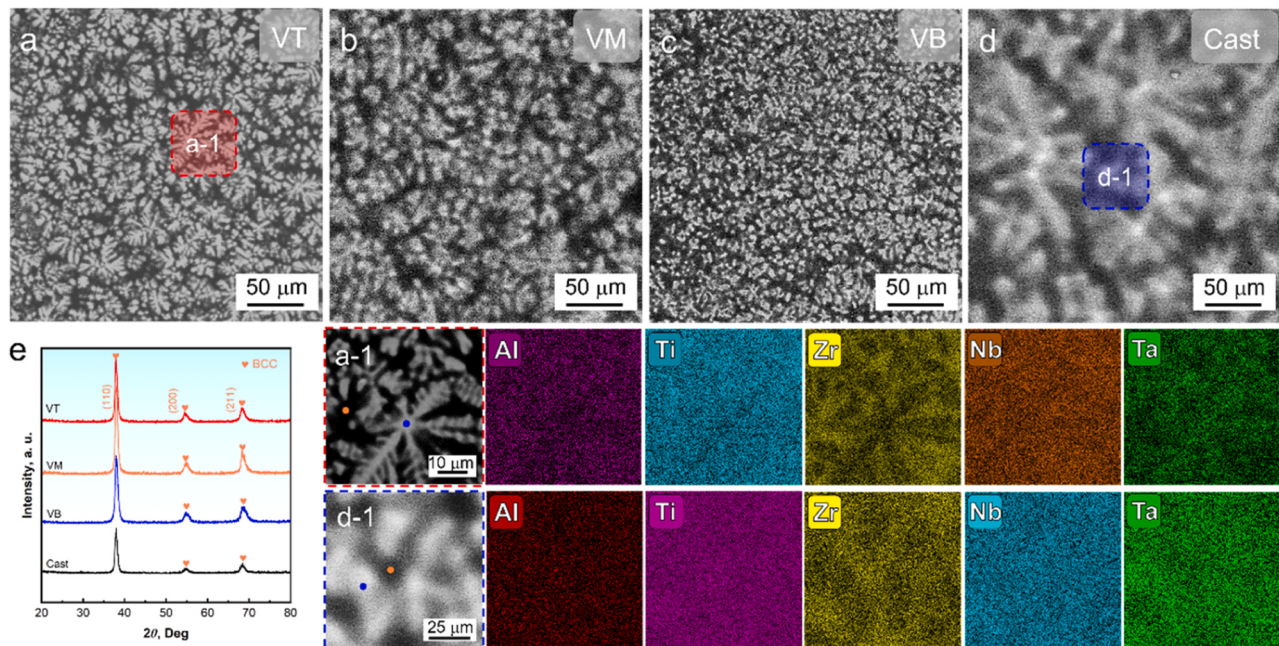


Fig. 4. (a-d) Backscatter electron (BSE) images of the LMD-fabricated alloy (VT, VM, and VB) and the as-cast alloys, where (a-1, d-1) are the EDS elemental maps of the corresponding regions in (a, d), respectively, (e) the XRD patterns of the LMD-fabricated and the as-cast alloys, respectively.

continuous matrix within the entire alloy, as presented in Fig. 6(a). Further, selected area electron diffraction (SAED) patterns along the $[110]_{\text{BCC}}$ zone axis and the corresponding dark-field (DF) image show that the cuboidal BCC nanoparticles (indicated by the white arrow) with a radius of $r \sim 3.5 \text{ nm}$ precipitated in the B2 matrix, as shown in Fig. 6(b),

c), where the cuboidal BCC nanoparticles and B2 matrix are with the volume fraction of $f \sim 65.1 \%$ and $f \sim 34.9 \%$, respectively. The high-resolution TEM (HRTEM) image and corresponding inverse Fourier transform (IFFT) pattern given in Fig. 6(d, d-1) indicate that the cuboidal BCC precipitates are perfectly coherent with the B2 matrix.

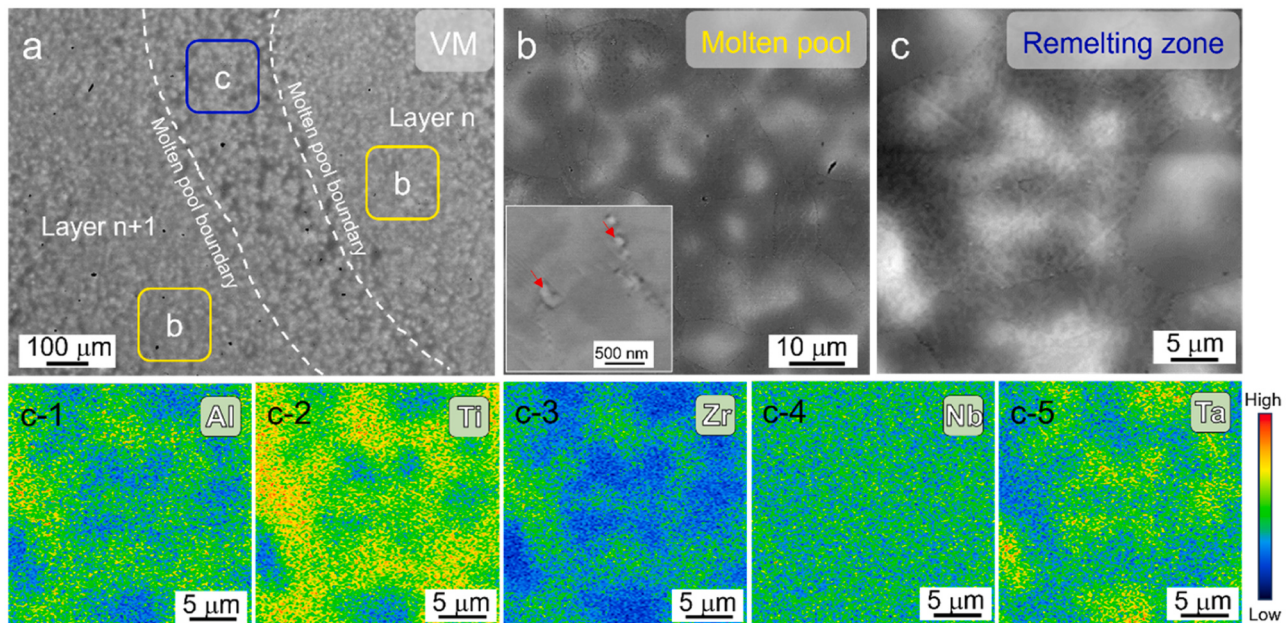


Fig. 5. (a) BSE image of molten pools and remelting zones in the VM sample of the LMD-fabricated alloy, (b) the magnified image of the molten pools, (c) the magnified image of the remelting zones and the corresponding EPMA elemental maps.

And the orientation relationship between BCC nanoparticles and B2 matrix can be described by $[110](00\bar{2})_{\text{BCC}}//[110](001)_{\text{B2}}$, where the BCC and B2 are with the lattice constant of $a_{\text{BCC}} \sim 0.3434 \text{ nm}$ and $a_{\text{B2}} \sim 0.3457 \text{ nm}$, respectively. Furthermore, the HAADF image and corresponding elemental maps and lines of Al, Ti, Zr, Nb, and Ta are presented in Fig. 6(a-1, a-2). It is found that the elemental segregation is not obvious and only BCC nanoparticles enriched in Nb and Ta elements can be observed, due to the small size of the BCC/B2 coherent microstructure. The specific compositions obtained by HAADF-STEM of the BCC nanoparticles and B2 matrix are measured to be $\text{Al}_{0.9}\text{Ti}_{35.4}\text{Zr}_{26.0}\text{Nb}_{13.3}\text{Ta}_{17.5}$ and $\text{Al}_{25.8}\text{Ti}_{37.3}\text{Zr}_{21.7}\text{Nb}_{9.1}\text{Ta}_{6.1}$ (at%, as listed in Table 3), respectively. It is found that the cuboidal BCC nanoparticles are enriched by Nb and Ta elements and the B2 matrix are segregated by a higher concentration of Al and Zr elements, where the ratio of Al and Zr in B2 matrix is approximately close to 1:1, while Ti elements are almost uniformly distributed in the BCC/B2 coherent microstructure. Moreover, the HAADF image and SAED pattern along the $[111]_{\text{BCC}}$ zone axis given in Fig. 7(a, b) indicate that the bright island-like nanoparticles (indicated by red arrows in the inset of Fig. 5 (b)) within the equiaxed grains are the BCC phase segregated by Nb and Ta (Fig. 7(a-1)). Besides, the island-like BCC nanoparticles also are precipitated at grain boundaries, as evidenced by Fig. 7(c, c-1) and Fig. S5.

In addition, to further clarify the microstructure of the as-cast alloy, the TEM analysis was also conducted, as shown in Fig. 7(d-f). It is found that there are no precipitates at the grain boundary in the as-cast alloy (Fig. 7(d)). The DF images and corresponding SAED patterns exhibit spherical B2 nanoparticles (nanocluster) with a size of 1 – 2 nm are dispersedly precipitated in the BCC matrix (Fig. 7(e, f)). In the case of as-cast alloy, obtaining the BCC/B2 coherent microstructure with cuboidal nanoparticles typically necessitates complex post-heat treatments processes. By contrast, the LMD technique offers distinct technological advantages by enabling the direct formation of the BCC/B2 coherent microstructure with cuboidal precipitates.

3.3. Mechanical properties

Fig. 8(a) gives compressive stress-strain curves at RT of the LMD-fabricated alloy and the as-cast alloy, and the data values are listed in

Table 4. The yield strength values of the LMD-fabricated alloys along vertical loading direction are $\sigma_{\text{YS}} = 1372 - 1573 \text{ MPa}$ obviously superior to that ($\sigma_{\text{YS}} = 1070 \text{ MPa}$) of the as-cast alloy, which is mainly attributed to the BCC/B2 coherent microstructure with cuboidal BCC nanoparticles precipitated. Also, the LMD-fabricated alloy has a good plasticity with a compression strain to fracture (δ) of 28 – 50 %. Notably, the mechanical properties of the LMD-fabricated alloy at the top (VT) and middle (VM) layers exhibit remarkable similarity, with values of ($\sigma_{\text{YS}} = 1382 \text{ MPa}$, 50 %) and ($\sigma_{\text{YS}} = 1372 \text{ MPa}$, 50 %), respectively, while the bottom layers (VB) show $\sigma_{\text{YS}} = 1573 \text{ MPa}$ and $\delta = 28 \%$. And the variation in microhardness (HV) values along the deposition direction exhibits a strong correlation with the evolution of yield strength, as shown in Fig. 8(b). The microhardness reaches its maximum value of 440 HV in the bottom layers, showing a rapid decreases with increasing deposition height, while the middle and top layers display lower microhardness of 390 – 400 HV. The underlying factors that govern the variation in mechanical properties will be discussed in the following section. Especially, the LMD-fabricated alloy exhibits isotropic mechanical properties at the same deposition height, as evidenced by the compressive curves of the LMD-fabricated alloy under horizontal loading direction (Fig. S6 and Table 4). Moreover, the compressive yield strength and compressive strain values at RT of the current LMD-fabricated alloy were compared with those of reported RHEAs fabricated by AM and arc-melting, as present in Fig. 8(c). It can be seen that the LMD-fabricated $\text{Al}_1\text{Ti}_5\text{Zr}_4\text{Nb}_3\text{Ta}_3$ alloy exhibits good strength-plasticity balance, even comparable to most existing RHEAs [12,13,30,31,40,41]. To explore the HT mechanical properties of the LMD-fabricated alloy, the compressive tests at the HT from 873 K to 1273 K were carried out, as displayed in Fig. 8(d). It is found that the current LMD-fabricated alloy demonstrates an excellent yield strength of $\sigma_{\text{YS}} = 1124 \text{ MPa}$ at 873 K, suggesting that the BCC/B2 coherent microstructure maintains remarkable thermal stability at elevated temperature. Then the yield strength decreases sharply to $\sigma_{\text{YS}} = 426 \text{ MPa}$ with the temperature up to 1073 K, which could be attributed to the transformation of BCC/B2 coherent microstructure to a single BCC solid solution result from a large solubility of alloying elements in solid solution structure. At 1273 K, the yield strength of $\sigma_{\text{YS}} = 259 \text{ MPa}$ can still be maintained.

To further clarify the fracture behavior of the LMD-fabricated alloy,

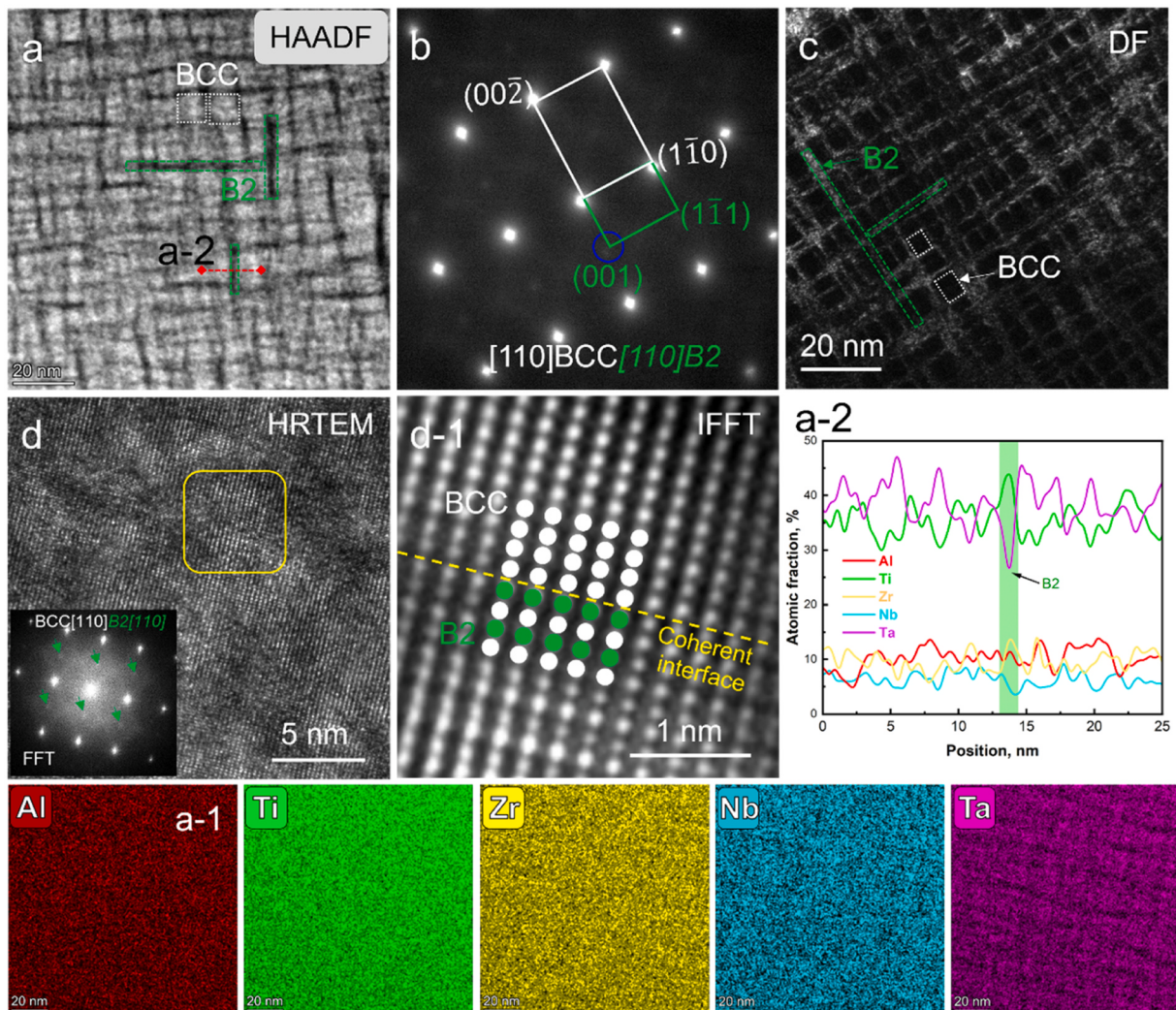


Fig. 6. TEM characterization of the VM sample. (a) HAADF image and corresponding elemental maps (a-1) and lines (a-2) of the BCC/B2 coherent microstructure, (b) SAED pattern along the $[110]_{\text{BCC}}$ zone axis and corresponding DF image, (d) HRTEM image and corresponding FFT pattern along the $[110]_{\text{BCC}}$ zone axis; (d-1) the corresponding IFFT pattern of yellow box area in (d).

the fracture surfaces of VB and HB samples were analyzed by SEM, as shown in Fig. 9(a, b). It is found that the fracture surfaces of these samples are comprised of massive shallow dimples and cleavage planes, indicating that ductile and brittle fracture simultaneously dominate fracture mechanism in the bottom samples. Consequently, it can be hypothesized that the mechanical properties of the current LMD-fabricated alloys change from brittle fracture to ductile fracture with the increase of deposition layers.

4. Discussion

4.1. The formation of the equiaxed grains

The formation of the textured grains induces anisotropic mechanical properties in AM-fabricated alloys, posing significant challenges for industrial applications [42]. However, the fine equiaxed grains with random grain orientations are obtained and uniformly distributed along the deposition direction in the present $\text{Al}_1\text{Ti}_5\text{Zr}_4\text{Nb}_3\text{Ta}_3$ alloy fabricated by LMD (Fig. 3(a-c)). According to the classical solidification theory, the morphology of grain is primarily governed by chemical composition of the alloy, the temperature gradient in solid/liquid interface (G) and solidification velocity (R) [43,44]. When the laser melting process, the metal powder absorbs sufficient laser energy and melts. Due to the

disparity in the melting point of the constituent elements in the $\text{Al}_1\text{Ti}_5\text{Zr}_4\text{Nb}_3\text{Ta}_3$ alloy, the high melting point Nb and Ta elements solidify first [45]. In this case, the high melting point elements are acted as heterogeneous nucleation sites, thereby promoting the instantaneous formation of equiaxed dendrites within the molten pool (Fig. 4(a-c)) [45, 46]. Moreover, a higher G/R value promotes the growth of columnar grains while a lower G/R value contributes the formation of equiaxed grains [44,46,47]. In the current study, the poor heat conductivity of the $\text{Al}_1\text{Ti}_5\text{Zr}_4\text{Nb}_3\text{Ta}_3$ RHEA results in a relatively low G value [44]. As the laser beam recedes from the molten pool surface, the extremely rapid solidification velocity (R) within the molten pool leads to a sufficiently low G/R value, thus facilitating the development of equiaxed grains in this work, as shown in Fig. 10(a). Besides, the fine equiaxed grains size can also be refined with the higher value of $G-R$ (Fig. 10(a)) [46]. During the deposition of the subsequent layers, although partial equiaxed grains undergo remelting due to laser beam, the relatively high laser scanning rate effectively reduces the penetration depth of the laser energy input, leading to the preservation of the majority of the equiaxed grains in the former layers. As a result, this LMD-fabricated alloy achieves a uniform distribution of equiaxed grains after undergoing thermal cycles.

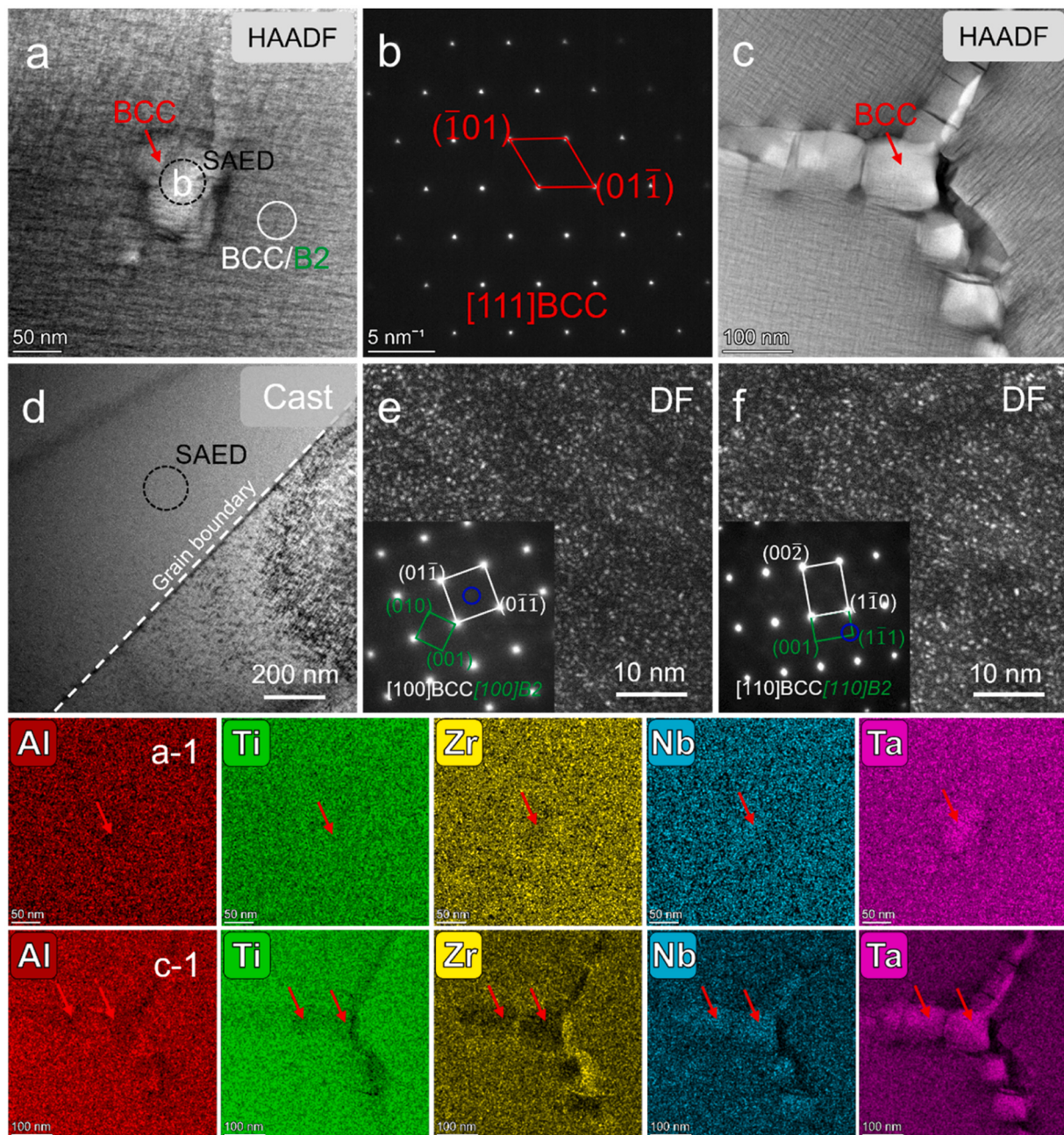


Fig. 7. TEM characterization of the LMD alloy (a-c) and the as-cast alloy (d-f). (a, a-1) HAADF image and corresponding elemental maps of the island-like BCC particles within the grain, (b) SAED pattern along the [111]_{BCC} zone axis of the island-like BCC particles, (c, c-1) HAADF and corresponding elemental maps of the island-like BCC particles at the grain boundary, (d) BF image, (e, f) DF images and corresponding SAED patterns along the [100]_{BCC} and [110]_{BCC} zone axis, respectively.

4.2. The formation of BCC/B2 coherent microstructure

Previous researches demonstrate that arc-melted RHEAs can be homogenized at 1473 – 1673 K, obtaining a “superalloy-like” microstructure composed of fine scale BCC and B2 phases in the subsequent heat treatment via spinodal decomposition [8, 14–17]. The critical factor for the formation of such a microstructure is believed to be subsequent water quenching [16]. In the current work, the ultrafast cool rate of the molten pool in LMD process reach up to 10^3 – 10^8 K·s⁻¹, which may have achieved same effects as water quenching [27]. In fact, the thermodynamic phase diagram calculation of the Al₁Ti₅Zr₄Nb₃Ta₃ alloy demonstrates that the high temperature phase (≥ 1000 K) is likely to be a single-phase BCC (Fig. 10(b)). In the cooling process, when the

temperature drops near to 873 K, the decomposition of the high temperature BCC phase (Fig. 10(b)) results in the formation of an interconnect network of BCC and B2 phases [16, 22]. There is sufficient evidence that Nb, Ta and Zr are likely responsible for the decomposition of the high temperature BCC phase during fast cooling due to a miscibility gap in Al-Ti-Zr-Nb-Ta alloy system [14]. The strong chemical interaction between Al and Zr with the largest enthalpy of formation ($\Delta H_{\text{mix}} = -43.7 \text{ kJ}\cdot\text{mol}^{-1}$) in the presence of Nb and Ta is likely responsible for the transformation of the BCC phase into a continuous ordered B2 phase enriched with Al and Zr during ultrafast cooling [14, 16]. In contrast, the Ti seems to be neutral in this reaction and tends to be uniformly distributed between these two phases [14]. The continuous change in the composition of the two phases during the cyclic thermal

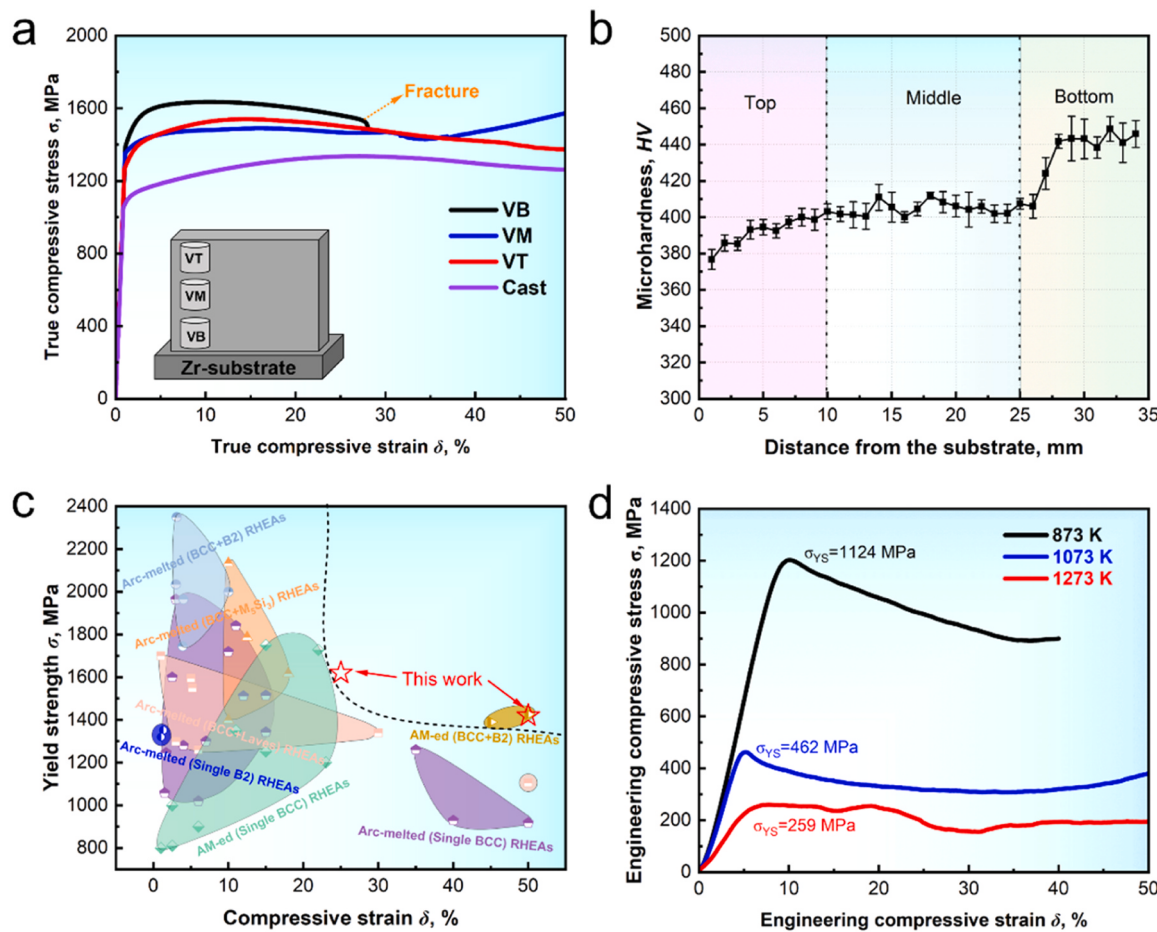


Fig. 8. Mechanical properties of the LMD-fabricated alloy and as-cast alloy. (a) The compressive true stress-strain curves of LMD-fabricated alloys under horizontal loading direction (displayed in the inset), (b) the microhardness values along the deposition direction in the single-wall sample of the LMD-fabricated alloy, (c) the compressive yield strength versus compressive strain of the LMD-fabricated alloy in comparison with those of arc-melted and additive manufactured RHEAs, (d) the compressive engineering stress-strain curves of the LMD-fabricated alloy at HT (873 K, 1073 K, and 1273 K).

Table 4

The RT compressive test date of the LMD-fabricated alloy under different loading direction and the as-cast alloy.

Alloy	Position	Yield strength, /MPa	Ultimate compressive strength, /MPa	Plasticity, /%
As-cast	/	1070	1338	50
LMD	VT	1382	1544	50
	VM	1372	1500	50
	VB	1573	1643	28
	HT	1319	1459	50
	HM	1300	1521	50
	HB	1625	1684	22

input in LMD process may further promotes the spinodal decomposition mechanism of phase transformation. More importantly, the morphology of cuboidal BCC nanoparticles should be dependent on a lattice misfit (ε) between BCC and B2 phases, where a moderate ε value of 0.4 – 0.8 % contributes to the formation of cuboidal nanoparticles in our previous work [33,48]. And the ε can be calculated by the equation of $\varepsilon = 2 \times (a_{B2} - a_{BCC}) / (a_{B2} + a_{BCC})$, in which a_{B2} and a_{BCC} are the lattice constants of B2 and BCC phases. Due to the reasonable cluster formula of Al₂M₁₄, a moderate ε value of ~ 0.64 % in the LMD-fabricated alloy contributes the cuboidal BCC nanoparticles to be dispersed into B2 matrix. Thus, the LMD process can generate the same effect of normal heat treatment, obtaining the BCC/B2 coherent microstructure with

cuboidal nanoparticles precipitated in the Al₁Ti₅Zr₄Nb₃Ta₃ RHEA. Furthermore, the extremely high cooling rate inhibits the diffusion of elements and effectively prevents the formation of brittle Al₃Zr₅ phase [24,33], which are believed that the B2 phase easily transform into stable Al₃Zr₅ phase thermodynamically along sub-grain and grain boundaries by the collapse of the {111} plane in B2 due to the close crystalline relationship [110](001)_{B2}||[120](211)_{Al₃Zr₅} between these phases at traditional aging process [49].

4.3. The differences in mechanical properties across the deposition layers

Analysis of the mechanical properties of the single-wall specimen of the LMD-fabricated alloy at different internal locations indicate that the alloy exhibits isotropic behavior at the same deposition height. However, the compressive yield strength and microhardness gradually decrease along the deposition direction from bottom layers to top layers (Fig. 8(a, b)). In particular, the mechanical properties of the bottom layers deviate significantly from those of the middle and top layers, while the latter two exhibit remarkable similarity. During the ultrafast melting and solidification process in the molten pool, thermal expansion and shrinkage of molten pool generally produce a local thermal strain and stress which induce dislocations (Fig. S2(d-f)) [50]. And the dynamic thermal cycling during the deposition of subsequent layers causes the accumulation of thermal stresses in former layers, thereby significant residual stress in the bottom layers [51,52]. The high residual stress in the bottom layers may combine with the loading during compression,

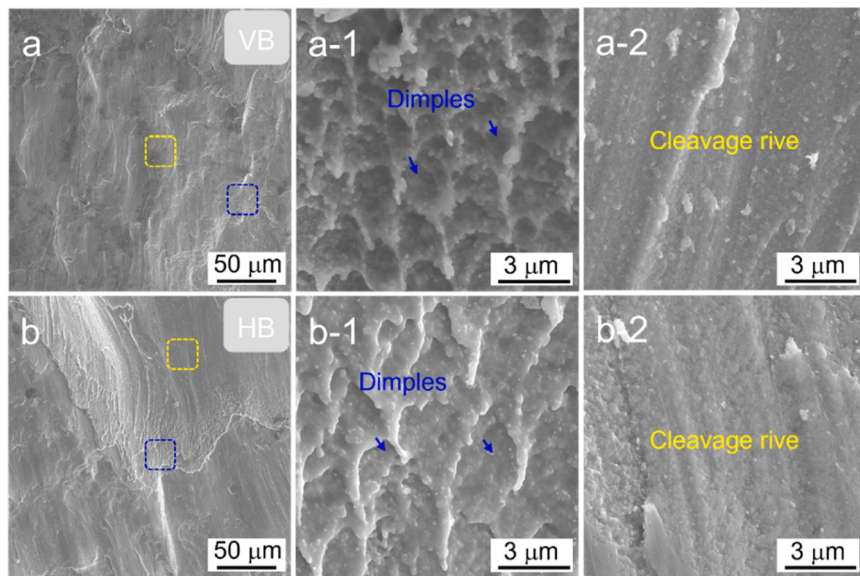


Fig. 9. The fracture surfaces of the deformed VB (a) and HB (b) samples of the LMD-fabricated alloys.

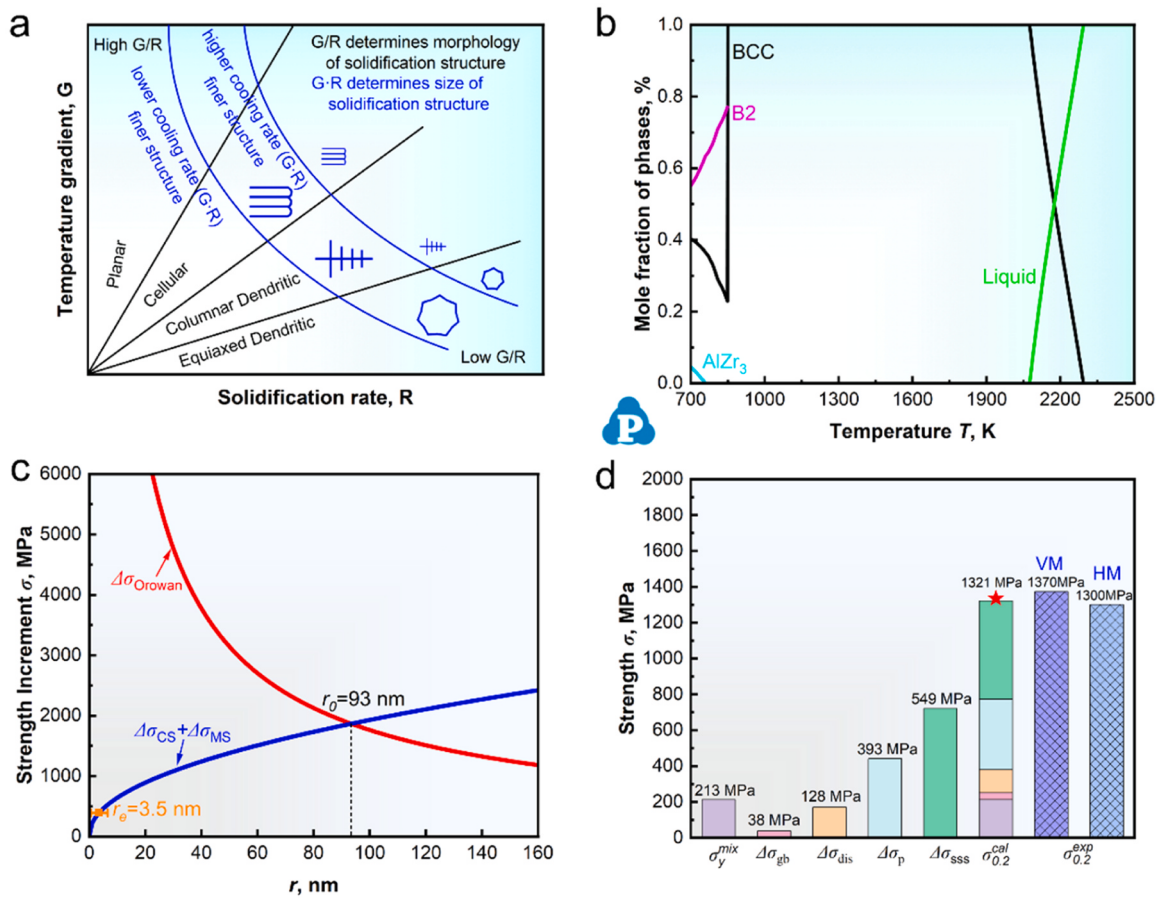


Fig. 10. (a) A schematic diagram of a solidification map showing grain morphology variation for different values of temperature gradient (G) and solidification rate (R), (b) the equilibrium phase diagrams of the $\text{Al}_1\text{Ti}_5\text{Zr}_4\text{Nb}_3\text{Ta}_3$ alloy, (c) the computations of $(\Delta\sigma_{\text{CS}} + \Delta\sigma_{\text{MS}})$ and $\Delta\sigma_{\text{Orowan}}$ as a function of particles size r for LMD-fabricated alloy, (d) the strength contributions offered from multiple strengthening mechanism in the LMD-fabricated alloy.

causing potential failure. More importantly, the bottom layers are subjected to the continuous thermal input, which may increase the volume fraction of island-like BCC precipitates at grain boundaries. The high volume fraction of island-like BCC precipitates promotes strength but

severely deteriorate the interfacial binding force of the grains in the bottom layers. Therefore, the large residual stresses and the high volume fraction of BCC precipitates at grain boundaries leads to the high strength of the bottom layers, while simultaneously inducing its

premature failure. In addition, the minor differences in mechanical properties of the middle and top layers, which may be attributed to the mitigated accumulation of residual stress and the more comparable microstructures.

4.4. The strengthening mechanisms

According to the above microstructure analysis of the representative VM samples of the LMD-fabricated alloy, the theoretical yield strength ($\sigma_{0.2}^{\text{cal}}$) of the VM samples can be expressed by adding the contributions from the grain boundary strengthening ($\Delta\sigma_{\text{gb}}$), dislocation strengthening ($\Delta\sigma_{\text{dis}}$), precipitation strengthening ($\Delta\sigma_p$), and solid solution strengthening ($\Delta\sigma_{\text{sss}}$). Hence, the yield strength ($\sigma_{0.2}^{\text{cal}}$) of the LMD-fabricated alloy can be expressed as:

$$\sigma_{0.2}^{\text{cal}} = \sigma_y^{\text{mix}} + \Delta\sigma_{\text{gb}} + \Delta\sigma_{\text{dis}} + \Delta\sigma_p + \Delta\sigma_{\text{sss}} \quad (4-1)$$

where σ_y^{mix} is the nominal yield strength of the LMD-fabricated alloy, which can be estimated using the rule of mixing [44], i.e. $\sigma_y^{\text{mix}} = \sum c_n (\sigma_y)_n = 213 \text{ MPa}$ where c_n is the concentration of n -th constituent element and $(\sigma_y)_n$ is the yield strength of this element as a pure metal. Basic information of the elements used is listed in Table 5.

The strength increment from grain boundary strengthening ($\Delta\sigma_{\text{gb}}$) referring to the classical Hall-Petch relationship [44]:

$$\Delta\sigma_{\text{gb}} = k_{\text{HP}} d^{-0.5} \quad (4-2)$$

where $d \sim 39 \mu\text{m}$ is the grain size of the VM sample, and k_{HP} represents the Hall-Petch coefficient at the RT , reported as $240 \text{ MPa } \mu\text{m}^{0.5}$ [44]. Therefore, the strength increment of $\Delta\sigma_{\text{gb}}$ is calculated to be 38 MPa .

Generally, the density of total dislocations consisted of statistically stored dislocations (SSDs) and geometrically necessary dislocations (GNDs) contributes to the dislocation strengthening ($\Delta\sigma_{\text{dis}}$) rather than that of GNDs alone. Thus, the contribution of total dislocations to $\Delta\sigma_{\text{dis}}$ can be estimated by Taylor model [53]:

$$\Delta\sigma_{\text{dis}} = M \alpha G b \sqrt{\rho_{\text{SSD}} + \rho_{\text{GND}}} \quad (4-3)$$

where the Taylor factor M and the dimensionless pre-factor α is 2.73 and 0.4 for the BCC materials, respectively [54]; $G = 38 \text{ MPa}$ is the shear modulus of the matrix, which can be estimated using the rule of mixing, according to Table 5; and $b = \frac{\sqrt{3}}{2} a_{\text{B2}} = 0.285 \text{ nm}$ is the Burgers vector. Previous researches indicate the density of the ρ_{SSD} often account for 15 % – 35 % of the total dislocation density [53]. Given the current alloy experienced the LMD process, the ρ_{SSD} could account for $\sim 25 \%$ of the total dislocation density in this alloy. Thus, based on the measured GND density of $\sim 0.88 \times 10^{14} \text{ m}^{-2}$ (Fig. S3(e)) in the VM sample, the SSD density of this alloy is $\sim 0.29 \times 10^{14} \text{ m}^{-2}$. Thus, the strength increment of $\Delta\sigma_{\text{dis}}$ is calculated to be 128 MPa .

The precipitation strengthening ($\Delta\sigma_p$) mechanism can be divided into two categories: the shearing mechanism and the Orowan bypassing mechanism. Shearing mechanism dominates the process of precipitation strengthening when the nanoparticles are small or coherent with the B2 matrix, the strength increment is determined by three factors, coherency strengthening ($\Delta\sigma_{\text{CS}}$), modulus mismatch strengthening ($\Delta\sigma_{\text{MS}}$), and ordering strengthening ($\Delta\sigma_{\text{OS}}$) [55]. Among them, the former two ($\Delta\sigma_{\text{CS}}$ and $\Delta\sigma_{\text{MS}}$) occur before dislocations shear the nanoparticles, while the

latter one ($\Delta\sigma_{\text{OS}}$) occurs during the shearing [55]. Thus, the larger value of ($\Delta\sigma_{\text{CS}} + \Delta\sigma_{\text{MS}}$) or $\Delta\sigma_{\text{OS}}$ determines strength increment produced by the shear mechanism. While the Orowan bypassing mechanism ($\Delta\sigma_{\text{Orowan}}$) dominates when the particle size is large enough or the particles are incoherent with the matrix. Since the two mechanisms occur concurrently and are independent of each other, the final strength increment is determined by the smaller value of dislocation shearing mechanisms or $\Delta\sigma_{\text{Orowan}}$. The equations available to calculate the strength increment from these two mechanisms are as follows [54,55]:

$$\Delta\sigma_{\text{CS}} = M \alpha_c (G e_c)^{\frac{3}{2}} \left(\frac{r f}{0.5 G b} \right)^{\frac{1}{2}} \quad (4-4)$$

$$\Delta\sigma_{\text{MS}} = 0.0055 M (\Delta G)^{\frac{3}{2}} \left(\frac{2f}{G} \right)^{\frac{1}{2}} \left(\frac{r}{b} \right)^{\frac{3m-1}{2}} \quad (4-5)$$

$$\Delta\sigma_{\text{OS}} = 0.81 M \frac{\gamma_{\text{APB}}}{2b} \left(\frac{3\pi f}{8} \right)^{\frac{1}{2}} \quad (4-6)$$

$$\Delta\sigma_{\text{Orowan}} = M \frac{0.4 G b}{\pi \sqrt{1-\nu}} \frac{\ln(2\sqrt{\frac{2}{3}}r/b)}{\lambda_p} \quad (4-7)$$

$$\lambda_p = 2\sqrt{\frac{2}{3}}r(\sqrt{\frac{\pi}{4f}} - 1) \quad (4-7-1)$$

where M is the Taylor factor for the BCC structure [33]; $\alpha_c = 2.6$; $m = 0.85$; $e_c = 2\varepsilon/3$ is the constrained lattice misfit [33]; G and $\Delta G = 6 \text{ GPa}$ are the shear modulus of the matrix and the shear modulus mismatch between BCC nanoparticles and matrix, respectively; b is the Burgers vector; $r = 3.5 \text{ nm}$ and $f = 65.1 \%$ are the average radius and the volume fraction of cuboidal BCC nanoparticles in the VM samples, respectively; $\gamma_{\text{APB}} = 0.11 \text{ J}\cdot\text{m}^{-2}$ is the antiphase boundary (APB) energy of the nanoparticles [56]; $\nu = 0.3$ is the Poisson ratio [33]; and λ_p is the inter-precipitate spacing. It is due to that ordering strengthening ($\Delta\sigma_{\text{OS}}$) of 373 MPa is lower than $\Delta\sigma_{\text{CS}} + \Delta\sigma_{\text{MS}}$ of 393 MPa , the $\Delta\sigma_{\text{CS}} + \Delta\sigma_{\text{MS}}$ will dominate the shearing mechanism. In addition, the variations of these strength increment with the particle size r are plotted in Fig. 10(c). When the particle size does not exceed the critical value (93 nm), the shearing mechanism will dominate precipitation strengthening (Fig. 10(c)). Thus, the strength increment from the cuboidal BCC nanoparticles is calculated to be $\Delta\sigma_p = \Delta\sigma_{\text{CS}} + \Delta\sigma_{\text{MS}} = 393 \text{ MPa}$.

The strength increment ($\Delta\sigma_{\text{sss}}$) from solute elements was calculated by the Curtin's solid solution strengthening model based on the interaction energy between solute atoms and dislocations. Here, $\Delta\sigma_{\text{sss}}$ is dependent on the zero-K yields shear stress (τ_{y0}) and the energy barrier (ΔE_b) for the thermally activated flow. The equations available to calculate the strength increment are as follows [57,58]:

$$\sigma_{\text{sss}}(T, \varepsilon) = M \tau_{y0} \left[1 - \left(\frac{KT}{\Delta E_b} \ln \frac{\varepsilon_0}{\varepsilon} \right)^{\frac{2}{3}} \right] \quad (4-8)$$

$$\tau_{y0} = A_r \alpha^{-\frac{1}{3}} G \left[\frac{1 + \nu}{1 - \nu} \right]^{\frac{4}{3}} \left[\frac{\sum_n c_n \Delta V_n^2}{b^6} \right]^{\frac{2}{3}} \quad (4-8-1)$$

$$\Delta E_b = A_E \alpha^{\frac{1}{3}} G b^3 \left[\frac{1 + \nu}{1 - \nu} \right]^{\frac{2}{3}} \left[\frac{\sum_n c_n \Delta V_n^2}{b^6} \right]^{\frac{1}{3}} \quad (4-8-2)$$

where M is the Taylor factor; $K = 1.380649 \times 10^{-23} \text{ J}\cdot\text{K}^{-1}$ is the Boltzmann constant; $\varepsilon = 10^4 \text{ s}^{-1}$ is a reference strain rate, while $\varepsilon_0 = 10^{-3} \text{ s}^{-1}$ is the finite strain rate; $\alpha = 0.0833$ and pre-factor coefficients $(A_r, A_E) = (0.04, 2.00)$ for BCC alloys; $T=298 \text{ K}$ is the thermodynamic temperature; b is the Burgers vector; c_n and $\Delta V_n = V_n - \bar{V}$ are the atomic concentration and misfit volume of the n -th ($n = 1, \dots, N$) solute element [59], in which $V_n = \frac{a_n^3}{2}$ is the atomic volume for the BCC

Table 5

Atomic radius (r), shear modulus (G), and yield strength ($\sigma_{0.2}$) of the pure metals.

Element/property	Al	Ti	Zr	Nb	Ta
r (nm)	0.143	0.146	0.155	0.143	0.143
G (Gpa)	26	44	33	38	69
$\sigma_{0.2}$ (MPa)	90	195	280	240	170

pure elements with lattice constants a_n and $\bar{V} = \sum_n c_n V_n$ is the atomic volume of the alloy, respectively; $G = \sum_n c_n G_n$ is the shear modulus of the alloy [59]. Basic information of the elements used is listed in Table 5. Therefore, the strength increments of $\Delta\sigma_{ss}$ is calculated to be 549 MPa.

In summary, the total strength contributions from each individual mechanism are plotted in Fig. 10(d). The calculated yield strength value ($\sigma_{0.2}^{cal}$) of 1321 MPa agrees well with the experimental yield strength value at the middle samples of the LMD-fabricated alloy.

5. Conclusion

In this work, the $\text{Al}_1\text{Ti}_5\text{Zr}_4\text{Nb}_3\text{Ta}_3$ lightweight RHEA was fabricated by LMD successfully using spherical pre-alloyed powder prepared by PREP. The microstructures and mechanical properties of $\text{Al}_1\text{Ti}_5\text{Zr}_4\text{Nb}_3\text{Ta}_3$ alloys fabricated by LMD and casting were investigated comparatively. The main conclusions are summarized as follows:

- (1) The LMD-fabricated alloy exhibits finer grains and a more uniform microstructure than the as-cast alloy, although both consist of equiaxed grains. This difference can be attributed to the rapid melting and solidification process derived from the short interaction time between the high-energy laser beam and powders.
- (2) The LMD process induces in-situ heat treatment and ultrafast cooling rate, which promotes the decomposition of the BCC phase and the formation of the BCC/B2 coherent microstructure. And the cuboidal BCC nanoparticles ($r \sim 3.5$ nm) are coherently precipitated in the B2 matrix, which is ascribed to a moderate lattice misfit ($\varepsilon \sim 0.64\%$) between BCC and B2 phases.
- (3) The LMD-fabricated alloy shows excellent yield strength of 1300 – 1600 MPa at RT, which is substantially better as compared to the as-cast alloy ($\sigma_{YS} = 1070$ MPa). The high yield strength of the LMD-fabricated alloy mainly derives from the grain boundary strengthening, dislocation strengthening, precipitation strengthening, and solid solution strengthening. Especially, the superior thermal stability of the BCC/B2 coherent microstructure endows it with excellent mechanical property at HT ($\sigma_{YS} = 1124$ MPa at 873 K and $\sigma_{YS} = 259$ MPa at 1273 K).
- (4) The LMD-fabricated alloy with high specific yield strength of $\sim 214 \text{ MPa}\cdot\text{g}^{-1}\cdot\text{cm}^3$ is comparable to most reported arc-melted and additively manufactured RHEAs, which has great potential in engineer applications.

CRediT authorship contribution statement

Xuanhong Cai: Investigation, Methodology, Conceptualization, Data curation, Formal analysis, Visualization, Writing – original draft. **Qiuju Yang:** Investigation, Visualization, Writing – review & editing. **Liufei Huang:** Investigation, Visualization. **Peilin Dong:** Investigation, Visualization. **Congcong Ren:** Investigation, Visualization. **YuanFeng Zhou:** Investigation, Visualization. **Jinfeng Li:** Funding acquisition, Supervision, Methodology, Writing – review & editing. **Qing Wang:** Funding acquisition, Supervision, Methodology, Writing – review & editing.

Declaration of Competing Interest

The authors declare that they have no known competing financial interests or personal relationships that could have appeared to influence the work reported in this paper.

Acknowledgements

This work was supported by the National Natural Science Foundation of China (52001288, 52171152, and U24A2024). The authors thank Fengyun Yu at Dalian University of Technology for help with SEM/

EPMA characterization and analysis.

Appendix A. Supporting information

Supplementary data associated with this article can be found in the online version at doi:10.1016/j.jallcom.2025.180312.

References

- [1] Z.F. Lei, X.J. Liu, Y. Wu, H. Wang, S.H. Jiang, S.D. Wang, X.D. Hui, Y.D. Wu, B. Gault, P. Kontis, Z.P. Lv, Enhanced strength and ductility in a high-entropy alloy via ordered oxygen complexes, *Nature* 563 (2018) 546–550.
- [2] D.B. Miracle, O.N. Senkov, A critical review of high entropy alloys and related concepts, *Acta Mater.* 122 (2017) 448–511.
- [3] L. Wang, J. Ding, S. Chen, K. Jin, Q. Zhang, J. Cui, B. Wang, B. Chen, T. Li, Y. Ren, Tailoring planar slip to achieve pure metal-like ductility in body-centred-cubic multi-principal element alloys, *Nat. Mater.* 22 (2023) 950–957.
- [4] S. Wei, S.J. Kim, J. Kang, Y. Zhang, Y. Zhang, T. Furuhara, E.S. Park, C.C. Tasan, Natural-mixing guided design of refractory high-entropy alloys with as-cast tensile ductility, *Nat. Mater.* 19 (2020) 1175–1181.
- [5] Z. Tian, W.P. Chen, H. Wang, C.L. Chu, J.C. Liu, L.Y. Hao, W. Xiong, J.M. Guo, Z. B. Jiao, Z.Q. Fu, Microstructural evolution, mechanical behavior, and deformation mechanisms of a lightweight Ti–Nb–Cr–V refractory high-entropy alloy at room and elevated temperatures, *Mater. Sci. Eng. A* 910 (2024) 146883.
- [6] L.F. Huang, Y.N. Sun, N. Chen, H.W. Luan, G.M. Le, X. Liu, Y.Q. Ji, Y.P. Lu, P. K. Liaw, X.S. Yang, Y.Z. Zhou, J.F. Li, Simultaneously enhanced strength-ductility of AlCoCrFeNi_{2.1} eutectic high-entropy alloy via additive manufacturing, *Mater. Sci. Eng. A* 830 (2022) 142327.
- [7] P.L. Dong, L. Zhang, L.F. Huang, Q. Yang, L. Li, L. Ma, Z.Y. Zhong, J.F. Li, Cooperative regulation of mechanical properties and magnetoresistance effect in high-entropy alloys by spinodal decomposition, *J. Alloy. Compd.* 970 (2024) 172547.
- [8] P.K. Kumar, S.J. Kim, Q. Yu, J. Ell, M. Zhang, Y. Yang, J.Y. Kim, H. Park, A.M. Minor, E.S. Park, Compressive vs. tensile yield and fracture toughness behavior of a body-centered cubic refractory high-entropy superalloy Al_{0.5}Nb_{1.25}Ta_{1.25}TiZr at temperatures from ambient to 1200° C, *Acta Mater.* 245 (2023) 118620.
- [9] Y.C. Li, M. Li, Q. Wang, Y.J. Zhao, S. Zhang, C.L. Zou, Y. Li, L.C. Wang, C. Dong, Composition optimization of Inconel 718 via cluster formula and experimental verification, *J. Mater. Sci. Technol.* 140 (2023) 249–259.
- [10] O.N. Senkov, G.B. Wilks, D.B. Miracle, C.P. Chuang, P.K. Liaw, Refractory high-entropy alloys, *Intermetallics* 18 (2010) 1758–1765.
- [11] O.N. Senkov, G.B. Wilks, J.M. Scott, D.B. Miracle, Mechanical properties of Nb₂₅Mo₂₅Ta₂₅W₂₅ and V₂₀Nb₂₀Mo₂₀Ta₂₀W₂₀ refractory high entropy alloys, *Intermetallics* 19 (2011) 698–706.
- [12] O.N. Senkov, D.B. Miracle, K.J. Chaput, J. Couzinie, Development and exploration of refractory high entropy alloys—A review, *J. Mater. Res* 33 (2018) 3092–3128.
- [13] Z. Wang, S. Chen, S. Yang, Q. Luo, Y. Jin, W. Xie, L. Zhang, Q. Li, Lightweight refractory high-entropy alloys: a comprehensive review, *J. Mater. Sci. Technol.* 151 (2023) 41–65.
- [14] O.N. Senkov, J.K. Jensen, A.L. Pilchak, D.B. Miracle, H.L. Fraser, Compositional variation effects on the microstructure and properties of a refractory high-entropy superalloy AlMo_{0.5}NbTa_{0.5}TiZr, *Mater. Des.* 139 (2018) 498–511.
- [15] O.N. Senkov, S. Gorsse, D.B. Miracle, High temperature strength of refractory complex concentrated alloys, *Acta Mater.* 175 (2019) 394–405.
- [16] V. Soni, B. Gwalani, T. Alam, S. Dasari, Y. Zheng, O.N. Senkov, D. Miracle, R. Banerjee, Phase inversion in a two-phase, BCC+B2, refractory high entropy alloy, *Acta Mater.* 185 (2020) 89–97.
- [17] J. Couzinie, M. Heczko, V. Mazánová, O.N. Senkov, M. Ghazisaeidi, R. Banerjee, M. J. Mills, High-temperature deformation mechanisms in a BCC–B2 refractory complex concentrated alloy, *Acta Mater.* 233 (2022) 117995.
- [18] O.N. Senkov, B. Crossman, S.I. Rao, J.P. Couzinie, D.B. Miracle, T.M. Butler, R. Banerjee, M. Mills, Mechanical properties of an Al₁₀Nb₂₀Ta₁₅Ti₃₀V₅Zr₂₀ A2/B2 refractory superalloy and its constituent phases, *Acta Mater.* 254 (2023) 119017.
- [19] V. Soni, O.N. Senkov, B. Gwalani, D.B. Miracle, R. Banerjee, Microstructural design for improving ductility of an initially brittle refractory high entropy alloy, *Sci. Rep.* 8 (2018) 8816.
- [20] K. Gao, Y. Chu, W. Zhou, Y. Tian, Y. Zhang, Y. Li, Phase inversion in a lightweight high Al content refractory high-entropy alloy, *J. Mater. Sci. Technol.* 150 (2023) 124–137.
- [21] A.C. Fan, Y.S. Chen, C.C. Chi, D.B. Miracle, J. Shieh, P.C. Kuo, C.H. Hsu, K.Ch. Yang, M.Y. Lu, M.H. Tsai, Stability of the B2 phase in Al-Nb-Ta-Ti-Zr refractory high-entropy superalloys: Resolving identification conflicts and offering practical solutions, *J. Alloy. Compd.* 1021 (2025) 179591.
- [22] T.E. Whitfield, E.J. Pickering, L.R. Owen, C.N. Jones, H.J. Stone, N.G. Jones, The effect of Al on the formation and stability of a BCC-B2 microstructure in a refractory metal high entropy superalloy system, *Materialia* 13 (2020) 100858.
- [23] O.N. Senkov, J. Couzinie, S.I. Rao, V. Soni, R. Banerjee, Temperature dependent deformation behavior and strengthening mechanisms in a low density refractory high entropy alloy Al₁₀Nb₁₅Ta₅Ti₃₀Zr₂₀, *Materialia* 9 (2020) 100627.
- [24] A. Sharma, S. Dasari, V. Soni, Z. Kloenne, J. Couzinie, O.N. Senkov, D.B. Miracle, S. G. Srinivasan, H. Fraser, R. Banerjee, B2 to ordered omega transformation during isothermal annealing of refractory high entropy alloys: implications for high temperature phase stability, *J. Alloy. Compd.* 953 (2023) 170065.

- [25] C. Yang, H. Bian, K. Aoyagi, Y. Hayasaka, K. Yamanaka, A. Chiba, Synergetic strengthening in HfMoNbTaTi refractory high-entropy alloy via disordered nanoscale phase and semicoherent refractory particle, *Mater. Des.* 212 (2021) 110248.
- [26] R. Feng, B. Feng, M.C. Gao, C. Zhang, J.C. Neufeind, J.D. Poplawsky, Y. Ren, K. An, M. Widom, P.K. Liaw, Superior high-temperature strength in a supersaturated refractory high-entropy alloy, *Adv. Mater.* 33 (2021) 2102401.
- [27] C. Han, Q. Fang, Y. Shi, S.B. Tor, C.K. Chua, K. Zhou, Recent advances on high-entropy alloys for 3D printing, *Adv. Mater.* 32 (2020) 1903855.
- [28] B. Su, Y.Y. Zhu, Y.S. Zhang, Z. Li, F. Cheng, S.S. Li, Deformation mechanisms of additively manufactured Hf₁₀Nb₁₂Ti₄₀V₃₈ refractory high-entropy alloy: dislocation channels and kink bands, *Mater. Sci. Eng. A* 915 (2024) 147247.
- [29] D. Cui, B. Guo, Z. Yang, X. Liu, Z. Wang, J. Li, J. Wang, F. He, Unraveling microstructure and mechanical response of an additively manufactured refractory TiVHfNbMo high-entropy alloy, *Addit. Manuf.* 84 (2024) 104126.
- [30] A. Chesetti, S. Banerjee, S. Dasari, M.S.K. Nartu, S.M. Varahabhatla, A. Sharma, A. Ramakrishnan, D. Satko, S. Gorsse, A. Salem, 3D printable low density B2+BCC refractory element based complex concentrated alloy with high compressive strength and plasticity, *Scr. Mater.* 225 (2023) 115160.
- [31] D. Ouyang, P. Zhang, C. Zhang, N. Li, K.C. Chan, L. Liu, High-strength lamellar high-entropy alloys in-situ synthesized by laser additive manufacturing, *Mater. Sci. Eng. A* 867 (2023) 144745.
- [32] B. Su, J. Li, C. Yang, Y. Zhang, Z. Li, Y. Zhang, Microstructure and mechanical properties of a refractory AlMn_{0.5}NbTa_{0.5}TiZr high-entropy alloy manufactured by laser-directed energy deposition, *Mater. Lett.* 335 (2023) 133748.
- [33] D. Jin, Z. Wang, J. Yuan, B. Jiang, F. Yu, J. Li, Q. Wang, High-strength and energetic Al₂Ti₆Zr₂Nb₃Ta₃ high entropy alloy containing a cuboidal BCC/B2 coherent microstructure, *J. Alloy. Compd.* 931 (2023) 167546.
- [34] Q. Wang, J. Han, Y. Liu, Z. Zhang, C. Dong, P.K. Liaw, Coherent precipitation and stability of cuboidal nanoparticles in body-centered-cubic Al_{0.4}Nb_{0.5}Ta_{0.5}TiZr_{0.8} refractory high entropy alloy, *Scr. Mater.* 190 (2021) 40–45.
- [35] X.H. Cai, Z.H. Wang, B. Niu, J.F. Li, Q. Wang, Microstructural evolutions and mechanical properties of energetic Al₁(TiZrNbTaMoCr)₁₅ high-entropy alloys, *Acta Metall. Sin. -Engl. Lett.* 37 (2024) 620–632.
- [36] Y.G. Dong, S. Chen, N.N. Jia, Q.H. Zhang, L. Wang, Y.F. Xue, K. Jin, Microstructures and mechanical properties of Ta-Nb-Zr-Ti-Al refractory high entropy alloys with varying Ta/Ti ratios, *Tungsten* 3 (2021) 406–414.
- [37] G. Chen, S.Y. Zhao, P. Tan, J. Wang, C.S. Xiang, H.P. Tang, A comparative study of Ti-6Al-4V powders for additive manufacturing by gas atomization, plasma rotating electrode process and plasma atomization, *Powder Technol.* 333 (2018) 38–46.
- [38] T. DebRoy, H.L. Wei, J.S. Zuback, T. Mukherjee, J.W. Elmer, J.O. Milewski, A. M. Beese, A.D. Wilson-Heid, A. De, W. Zhang, Additive manufacturing of metallic components-process, structure and properties, *Prog. Mater. Sci.* 92 (2018) 112–224.
- [39] T. Mukherjee, J.W. Elmer, H.L. Wei, T.J. Lienert, W. Zhang, S. Kou, T. DebRoy, Control of grain structure, phases, and defects in additive manufacturing of high-performance metallic components, *Prog. Mater. Sci.* 138 (2023) 101153.
- [40] H. Wang, P.Y. Yang, W.J. Zhao, S.H. Ma, J.H. Hou, Q.F. He, C.L. Wu, H.A. Chen, Q. Wang, Q. Cheng, B.S. Guo, J.C. Qiao, W.J. Lu, S.J. Zhao, X.D. Xu, C.T. Liu, Y. Liu, C.W. Pao, Y. Yang, Lattice distortion enabling enhanced strength and plasticity in high entropy intermetallic alloy, *Nat. Commun.* 15 (2024) 6782.
- [41] A. Jarlöv, Z.G. Zhu, W.M. Ji, S.B. Gao, Z.H. Hu, P. Vivegananthan, Y.J. Tian, D. R. Kripalani, H.Y. Fan, H.L. Seet, C.J. Han, L.M. Tan, F. Liu, M.L.S. Nai, K. Zhou, Recent progress in high-entropy alloys for laser powder bed fusion: design, processing, microstructure, and performance, *Mater. Sci. Eng. R.* 161 (2024) 100834.
- [42] Y. Kok, X.P. Tan, P. Wang, M.L.S. Nai, N.H. Loh, E. Liu, S.B. Tor, Anisotropy and heterogeneity of microstructure and mechanical properties in metal additive manufacturing: A critical review, *Mater. Des.* 139 (2018) 565–586.
- [43] V.P.N. Samy, M. Schäfele, F. Brasche, U. Krupp, C. Haase, Understanding the mechanism of columnar-to-equiaxed transition and grain refinement in additively manufactured steel during laser powder bed fusion, *Addit. Manuf.* 73 (2023) 103702.
- [44] S.Y. Gou, M.Y. Gao, Y.Z. Shi, S.C. Li, Y.T. Fang, X.H. Chen, H.C. Chen, W. Yin, J. B. Liu, Z.F. Lei, H.T. Wang, Additive manufacturing of ductile refractory high-entropy alloys via phase engineering, *Acta Mater.* 248 (2023) 118781.
- [45] S. Mooraj, G. Kim, X. Fan, S. Samuha, Y.J. Xie, T.Y. Li, J.S. Tiley, Y. Chen, D.J. Yu, K. An, P. Hosemann, P.K. Liaw, W. Chen, W. Chen, Additive manufacturing of defect-free TiZrNbTa refractory high-entropy alloy with enhanced elastic isotropy via in-situ alloying of elemental powders, *Commun. Mater.* 5 (2024) 14.
- [46] Z.Y. Liu, D.D. Zhao, P. Wang, M. Yan, C. Yang, Z.W. Chen, J. Lu, Z.P. Lu, Additive manufacturing of metals: microstructure evolution and multistage control, *J. Mater. Sci. Technol.* 100 (2022) 224–236.
- [47] M. Bermingham, D. StJohn, M. Easton, L. Yuan, M. Dargusch, Revealing the mechanisms of grain nucleation and formation during additive manufacturing, *JOM* 72 (2020) 1065–1073.
- [48] Y. Ma, Q. Wang, B.B. Jiang, C.L. Li, J.M. Hao, X.N. Li, C. Dong, T.G. Nieh, Controlled formation of coherent cuboidal nanoprecipitates in body-centered cubic high-entropy alloys based on Al₂(Ni, Co, Fe, Cr)₁₄ compositions, *Acta Mater.* 147 (2018) 213–225.
- [49] N.Y. Yurchenko, N.D. Stepanov, S.V. Zherebtsov, M.A. Tikhonovsky, G. A. Salishchev, Structure and mechanical properties of B2 ordered refractory AlNbTiVZr_x (x = 0–1.5) high-entropy alloys, *Mater. Sci. Eng. A* 704 (2017) 82–90.
- [50] S. Tekumalla, M. Seita, S. Zaeferer, Delineating dislocation structures and residual stresses in additively manufactured alloys, *Acta Mater.* 262 (2024) 119413.
- [51] Y. Tian, Y.Z. Lu, R.L. Narayan, Optimization of tensile properties and anisotropy in a cryogenically treated laser additively manufactured high entropy alloy, *Int. J. Plast.* (2024) 104015.
- [52] H.G. Li, Y.J. Huang, J.F. Sun, Y.Z. Lu, The relationship between thermo-mechanical history, microstructure and mechanical properties in additively manufactured CoCrFeMnNi high entropy alloy, *J. Mater. Sci. Technol.* 77 (2021) 187–195.
- [53] D.D. Zhang, J.Y. Zhang, J. Kuang, G. Liu, J. Sun, The B2 phase-driven microstructural heterogeneities and twinning enable ultrahigh cryogenic strength and large ductility in NiCoCr-based medium-entropy alloy, *Acta Mater.* 233 (2022) 117981.
- [54] T.Y. Han, J.Y. Chen, Z.F. Wei, N. Qu, Y. Liu, D.N. Yang, S.C. Zhao, Z.H. Lai, M. Jiang, J.C. Zhu, Effect of cooling rate on microstructure and mechanical properties of AlCrFe₂Ni₂ medium entropy alloy fabricated by laser powder bed fusion, *J. Mater. Res. Technol.* 25 (2023) 4063–4073.
- [55] Y.C. Li, J.Y. Pang, Z. Li, Q. Wang, Z.H. Wang, J.L. Li, H.W. Zhang, Z.B. Jiao, C. Dong, P.K. Liaw, Developing novel low-density high-entropy superalloys with high strength and superior creep resistance guided by automated machine learning, *Acta Mater.* 285 (2025) 120656.
- [56] B. Dou, Y. Pan, S.E. Liu, B.P. Wang, B. Cheng, L. Wang, S.H. Sun, Y.F. Xue, Achieving outstanding strength-ductility matching in BCC light-weight high entropy alloys via high content ordered nanoprecipitates, *Mater. Sci. Eng. A* 889 (2024) 145861.
- [57] F. Maresca, W.A. Curtin, Mechanistic origin of high strength in refractory BCC high entropy alloys up to 1900K, *Acta Mater.* 182 (2020) 235–249.
- [58] C. Varvenne, A. Luque, W.A. Curtin, Theory of strengthening in fcc high entropy alloys, *Acta Mater.* 118 (2016) 164–176.
- [59] M.L. Han, Y. Wu, X.B. Zong, Y.Z. Shen, X.B. Zhang, Q.S. Zeng, Z.P. Lu, Lightweight single-phase Al-based complex concentrated alloy with high specific strength, *Nat. Commun.* 15 (2024) 7102.